ACS OMEGA

http://pubs.acs.org/journal/acsodf

Article

Formation Mechanism of Fibrous Web in the Solution Blowing Process

Guangwu Sun, Yudong Wang,* Yinjiang Zhang, Wanli Han, and Shanshan Shang

Cite This: *ACS Omega* 2022, 7, 20584−20595

Read Online

ACCESS | Metrics & More | Article Recommendations

ABSTRACT: Solution blowing (SB) is a widely reported technology that can be used to fabricate fibers at the micro- and nanoscale. To reveal the fibrous web formation mechanism in SB, we improved our previous melt blowing (MB) model to predict fibrous web structures. Then, we fabricated two samples and simulated the same number of virtual samples in the computer to verify the model. Thereafter, we measured the structural parameters including the fiber diameter, fiber orientation, basis weight, and pore size. Our model provides a good prediction of the fiber orientation and basis weight. However, the predicted fiber diameter was slightly smaller than the measured diameter. The experimental pore size distribution was also different from that in the simulated results. The model provides a virtual fabrication process to reveal a fibrous web formation mechanism and finds a similar distribution of these structural parameters between SB and MB.

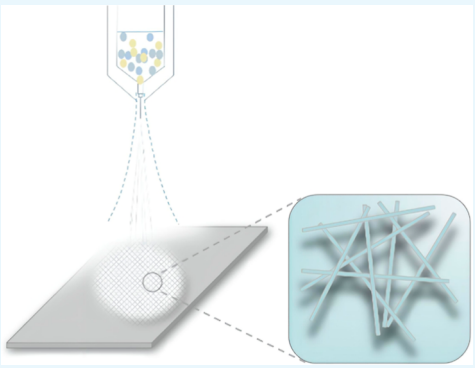

1. INTRODUCTION

Solution blowing (SB) is kindred to melt blowing (MB). The former still exists in the laboratory, while the latter has been applied in our daily lives. Compared with MB, a functional precursor solution is always employed in the SB process to produce functional fibers. Many articles have reported the fabrication of functional fibers and the application of SB products. For instance, Farias[1] reported a crack-free mullite fibrous web, Li[2] fabricated a submicrometric alumina fibrous mat, Zhuang[3] produced a cellulose fibrous film, and Rajgarhia[4] introduced evaporation-induced phase separation technology into SB and fabricated a bicomponent fibrous mat [polyvinyl acetate and polyvinylpyrrolindone (PVP)] with a core−shell, bilobal, and interpenetrating network morphology. In addition, a polylactic acid (PLA) fiber,[5,6] PVP fiber,[5] soy protein fiber,[7] ethylene-co-vinyl acetate fiber,[8] and some other functional fibers[9−11] fabricated by SB have been reported.

To the best of our knowledge, theoretical research on fiber formation by SB has been rarely reported. Only Sinha-Ray[12] presented a numerical model of fiber formation by SB. However, they only reported the prediction of fiber diameter distribution. Other structural parameters including the pore size, fiber orientation, and basis weight were not predicted. In this study, we improved the previous model of MB[13−15] and employed it to study web formation and predict the web structure in the SB process. The remainder of the paper is organized as follows. The theoretical aspects of this study are discussed in Section 2. Section 3 describes the experimental setup. The results are presented and discussed in Section 4, and the conclusions are drawn in Section 5.

2. THEORETICAL DESCRIPTION

This section is divided into three subsections. The derivation of the theoretical formulas is discussed in Section 2.1. Section 2.2 describes the air flow simulation using ANSYS software. The calculation of the web structural parameters is presented in Section 2.3.

2.1. Numerical Model. The following assumptions should be stated prior to describing the numerical equations:

1. The entanglement between fibers is ignored.
2. The entire model is only applicable for simulating a thin web and not the fiber stack effect.
3. The fiber movement mode on the collector is slide rather than roll.
4. Evaporation is a linear process from the nozzle to the collector. Thus, the evaporation rate of the solvent is constant.
5. The evaporation of solvent has no effect on the density and viscosity of the solution.
6. The solvent is fully evaporated when the fiber attaches to the collector.
7. The movement of the collector does not affect the air flow on the collector.

Received: January 13, 2022
Accepted: May 19, 2022
Published: June 8, 2022

https://doi.org/10.1021/acsomega.2c00276
ACS Omega 2022, 7, 20584−20595

8. Once the solution drop attaches to the collector, it immediately solidifies into a fiber. The phase transformation of the fiber is ignored.

In our previous model,[13] the solution comprised a series of solution segments. In each solution segment, two beads were connected by a Maxwell model component (a Newton dashpot and a hook spring), as shown in Figure 1. Each solution

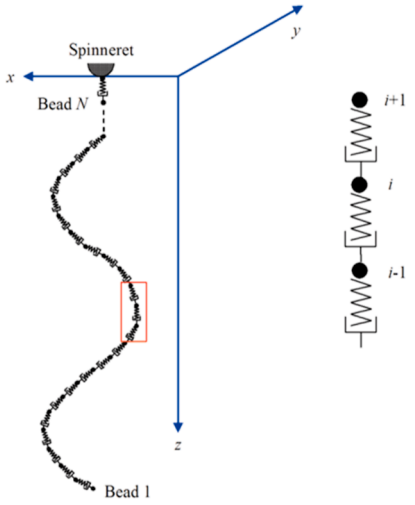

Figure 1. Solution model schematic diagram.

segment can be easily stretched or bent. When the molten polymer was extruded from the nozzle, it was driven and stretched by air drag ($\mathbf{F}_d$) and gravity ($\mathbf{G}$). Meanwhile, the viscoelastic force ($\mathbf{F}_{ve}$) and surface tension ($\mathbf{F}_b$) inside the solution resisted the solution deformation. Thus, the governing equation of the solution dynamics in the air jet is given by

$$m_{i-1,i}\frac{\mathrm{d}^2\mathbf{r}_{i-1,i}}{\mathrm{d}t^2} = \mathbf{F}_{d,i-1,i} + \mathbf{F}_{vei,i-1,i} + \mathbf{F}_{b,i-1,i} + \mathbf{G}_{i-1,i} \quad (1)$$

Once the solution is deposited on the collector, the latter exerts friction ($\mathbf{F}_s$) on the solution. Thus, the governing equation can be expressed as[15]

$$m_{i-1,i}\frac{\mathrm{d}^2\mathbf{r}_{i-1,i}}{\mathrm{d}t^2} = \mathbf{F}_{d,i-1,i} + \mathbf{F}_{vei,i-1,i} + \mathbf{F}_{b,i-1,i} + \mathbf{F}_{s,i-1,i} + \mathbf{G}_{i-1,i} \quad (2)$$

These forces could be expressed as

$$\mathbf{F}_{d,i-1,i} = \mathbf{F}_{d,t,i-1,i} + \mathbf{F}_{d,n,i-1,i} \quad (3)$$

$$\mathbf{F}_{d,t,i-1,i} = \frac{1}{2}\pi d_{i-1,i} l_{i-1,i} C_f \rho_a (v_{a,t,i-1,i} - v_{f,t,i-1,i})^2 \quad (3\text{-}1)$$

$$\mathbf{F}_{d,n,i-1,i} = \frac{1}{2} d_{i-1,i} l_{i-1,i} C_{dn} \rho_a (\mathrm{v}_{a,n,i-1,i} - \mathrm{v}_{f,n,i-1,i})^2 \quad (3\text{-}2)$$

$$\mathbf{F}_{b,i-1,i} = \frac{\psi\pi d_{i-1,i}^2 k_{i-1,i}}{4\left(\frac{(x_{i-1}+x_i)^2}{2} + \frac{(y_{i-1}+y_i)^2}{2}\right)^{1/2}}\left(\left|\frac{x_i + x_{i-1}}{2}\right| \mathrm{sign}\left(\frac{x_{i-1}+x_i}{2}\right)\mathrm{i} + \left|\frac{y_i + y_{i-1}}{2}\right| \mathrm{sign}\left(\frac{y_{i-1}+y_i}{2}\right)\mathrm{j}\right) \quad (4)$$

$$\mathbf{F}_{v,i-1,i} = \frac{\pi d_{i-1,i}^2}{4}\boldsymbol{\sigma}_{i-1,i}\left(\frac{x_i - x_{i-1}}{l_{i-1,i}}\mathrm{i} + \frac{y_i - y_{i-1}}{l_{i-1,i}}\mathrm{j} + \frac{z_i - z_{i-1}}{l_{i-1,i}}\mathrm{k}\right) \quad (5)$$

$$\mathbf{F}_{s,i-1,i} = \gamma_{i-1,i}(\mathbf{F}_{z,i-1,i} + m_{i-1,i}g) \quad (6)$$

$k_{i-1,i}$ in eq 3-1 is the curvature of the solution segment $(i-1,i)$ and is given by

$$k_{i-1,i} = \frac{1}{2}(k_{i-1} + k_i) = \frac{1}{2}(\mathbf{r}'_{i-1} \times \mathbf{r}''_{i-1} + \mathbf{r}'_i \times \mathbf{r}''_i) \quad (7)$$

$\boldsymbol{\sigma}$ in eq 3-2 is the tensile stress, which is given by

$$\frac{\mathrm{d}\boldsymbol{\sigma}_{i-1,i}}{\mathrm{d}t} = E\frac{1}{l_{i-1,i}}\frac{\mathrm{d}l_{i-1,i}}{\mathrm{d}t} - \frac{E}{\mu_f}\boldsymbol{\sigma}_{i-1,i} \quad (8)$$

$\mathbf{F}_z$ in eq 4 is the press generated by the air flow in the z-direction (perpendicular to the collector) and can be expressed as

$$\mathbf{F}_{z,i-1,i} = \frac{1}{2} d_{i-1,i} l_{i-1,i} C_{dn} \rho_a (v_{a,z,i-1,i})^2 \quad (9)$$

In addition, the mass of the solution segment $(i-1,i)$ is expressed as follows

$$m_{i-1,i} = \frac{1}{4}\pi\rho_f d_{i-1,i}^2 l_{i-1,i} \quad (10)$$

On the other hand, evaporation will affect the mass of the solution. Thus, the mass of the solution segment $(i\text{-}1,i)$ is also given by

$$m_{i-1,i} = m_0(1 - e_r z_{i-1,i}) \quad (11)$$

In the above equations, the subscript $(i\text{-}1,i)$ represents the solution segment $(i\text{-}1,i)$, which comprises beads i and i-1; m, ρ_f, d, and l are the mass, density, diameter, and length of the solution segment, respectively; C_f and C_{dn} are the air drag coefficient and air press coefficient between the solution and air, respectively; ρ_a is the density of air; $\mathbf{v}$ represents the velocity; the subscripts t and n denote the radial and axial components, respectively; the subscripts a and f indicate air and solution, respectively; ψ is the bending force coefficient; γ is the friction coefficient between the fiber and collector; the superscript $'$ in eq 5 signifies a first-order derivative and $''$ represents a second-order derivative; $\mathbf{r}$ is the spatial vector of the bead, which equals to (x,y,z); E and μ are the elasticity modulus and dynamic viscosity, respectively; the subscript z denotes the component in the z-direction; m_0 is the initial solution mass, which is determined by the throughput rate; and e_r is the evaporation rate, which is measured by the SB experiment.

In this study, the air velocity should be simulated in advance. In some of the published simulations,[16−22] the fluent module of ANSYS software was employed to simulate the air velocity. To simulate the fibrous web on the collector, once the free end of the solution reached a given XY plane (a hypothetical collector), its XZ coordinates and diameter were frozen, whereas its Y coordinate was varied following the translational motion of the collector in the Y direction. The model achieved its solution in an iterative algorithm using MATLAB software. We have provided the solution protocol in our previous

https://doi.org/10.1021/acsomega.2c00276
ACS Omega 2022, 7, 20584−20595

articles.[14−16] To calculate the structural parameters of the fibrous web, the program should export the fiber position on the collector, as well as the fiber mass and diameter. The solution procedure of these numerical equations has been reported in our previous work[13−15] and is not discussed in this article (Table 1).

Table 1. Parameters Applied in the Model

parameters	symbol	value
solution density (PAN/DMAC)	ρ_f	0.92 g/mL
bending force coefficient of solution (PAN/DMAC)	Ψ	0.7 kg/s^2[a]
elasticity modulus of solution (PAN/DMAC)	E	40 Pa[b]
dynamic viscosity of solution (PAN/DMAC)	μ_f	26 Pa•s[b]
friction coefficient of a fiber (PAN)	Γ	4.3[c]

[a]The bending force coefficient of the solution is difficult to measure; instead, we applied the bending force coefficient from our previous work (ref 15). [b]Cited from ref 23. [c]Quoted from ref 24 which reported the friction coefficient of a PAN mat as an approximation owing to a rare report of a single PAN fiber.

2.2. Finite Element Simulation of Air Flow. The SB nozzle is shown in Figure 2a. Its internal flow channel was drawn using ANSYS software (2021R1, ANSYS. Inc., United States) and is displayed in Figure 2b. The entire computational domain and mesh are shown in Figure 3. The mesh comprised tetrahedrons in the mesh component system of ANSYS software. Approximately 0.1 million nodes and 0.6 million elements were included in the final mesh. The entire mesh was then imported into the fluent component system. To the best of our knowledge, the turbulence model of the air jet of SB has not yet been reported. Krutka[22] reported a turbulence model of MB. We introduce their recommendations directly. Thus, the standard k-epsilon was used as the viscous model, and C1-epsilon and C2-epsilon were 1.20 and 2.05, respectively. Owing to the high speed, the air density and viscosity are not constant. In the fluent component system, we chose the Clapeyron equation to describe the air density and Sutherland's law to calculate the air viscosity. The default algorithm, the press-velocity-coupled algorithm, was applied to solve the project. The solution was initialized by hybrid initialization with default settings. The condition of convergence was that the residual should be smaller than 0.001. Two samples were fabricated to verify the simulation. The two samples were produced under different conditions, as shown in Table 2. The boundary conditions should be consistent with the fabrication conditions. The details of the boundary conditions are as follows:

Inlet: The inlet was drawn as a circular plane where the compressed air collided in the computational domain. The pressure of the inlet was 0.5 MPa and 0.15 MPa.

Outlet: Four planes that connect with the atmospheric conditions; the pressure was identical to the atmospheric pressure.

Wall 1: The part of the nozzle.

Wall 2: The collector.

The obtained air velocity was used to calculate $\mathbf{v}_a$ in eq 3. The predicted velocity of the air flow is displayed in Section 4.1.

2.3. Structural Parameter Calculations. The structural parameters in this study include the fiber diameter, fiber orientation, basis weight, and pore size. The fiber diameter can be directly calculated using eq 3. In terms of the fiber orientation, the angle θ between each fiber segment and the cross direction (CD, the direction perpendicular to the collector movement) is calculated using the following equation

$$\theta = \arctan\left|\frac{y_i - y_{i-1}}{x_i - x_{i-1}}\right| + \frac{\pi}{2} \tag{12}$$

The added $\pi/2$ was used to enhance the angle range of [0, 180°]; x and y are the bead coordinates of the collector.

To evaluate the basis weight distribution, the entire fibrous web was separated into several rectangular pieces with the same area. The basis weight of each piece is the sum of the weight of all the fiber segments in the piece. Equation 10 reflects the description.

$$\mathrm{BW} = \pi\rho_f \sum_{i=1}^{n}\left(\frac{d_{i-1,i}}{2}\right)^2 l_{i-1,i} \tag{13}$$

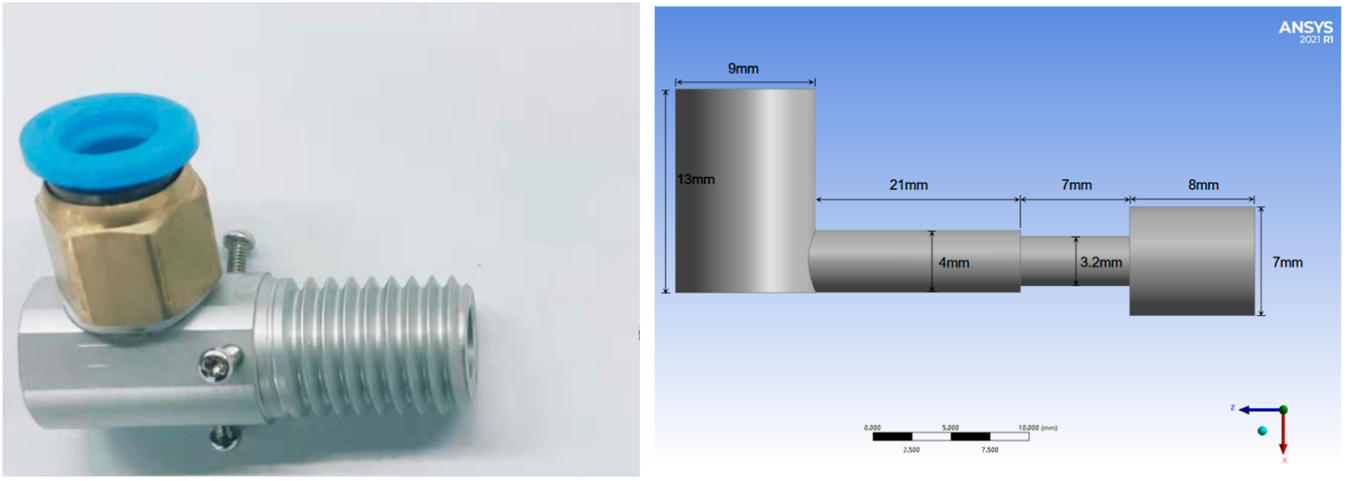

Figure 2. SB nozzle: (a) photograph and (b) three-dimensional (3D) model.

https://doi.org/10.1021/acsomega.2c00276
ACS Omega 2022, 7, 20584−20595

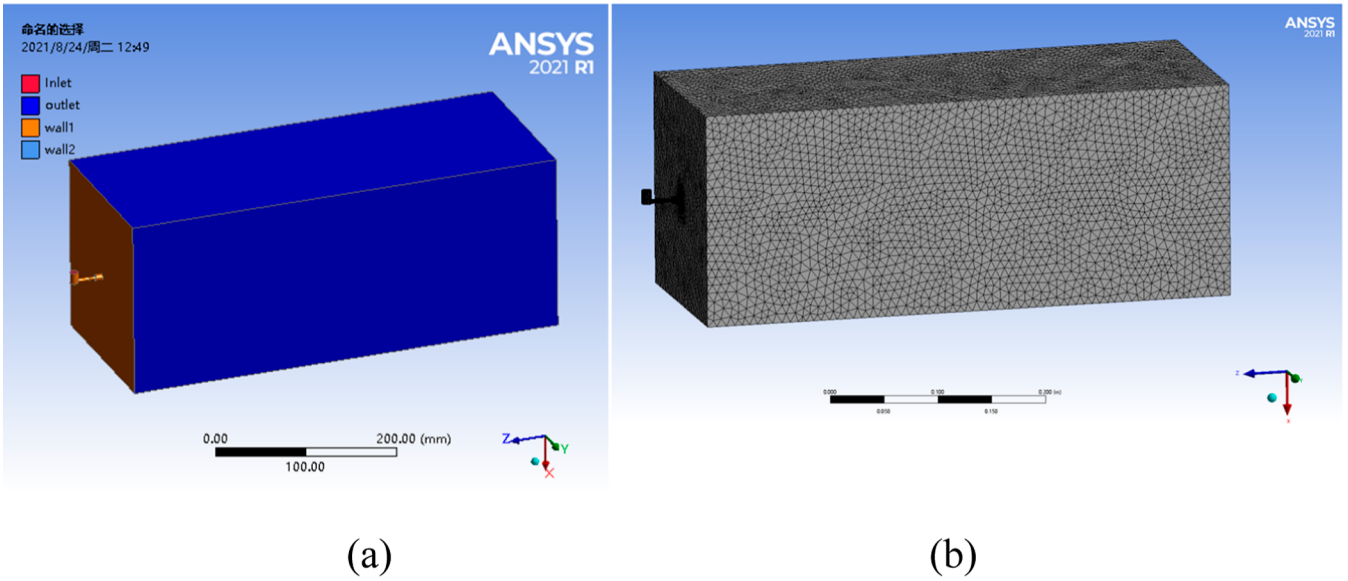

Figure 3. Computational domain of the air flow in SB: (a) 3D model and (b) mesh model.

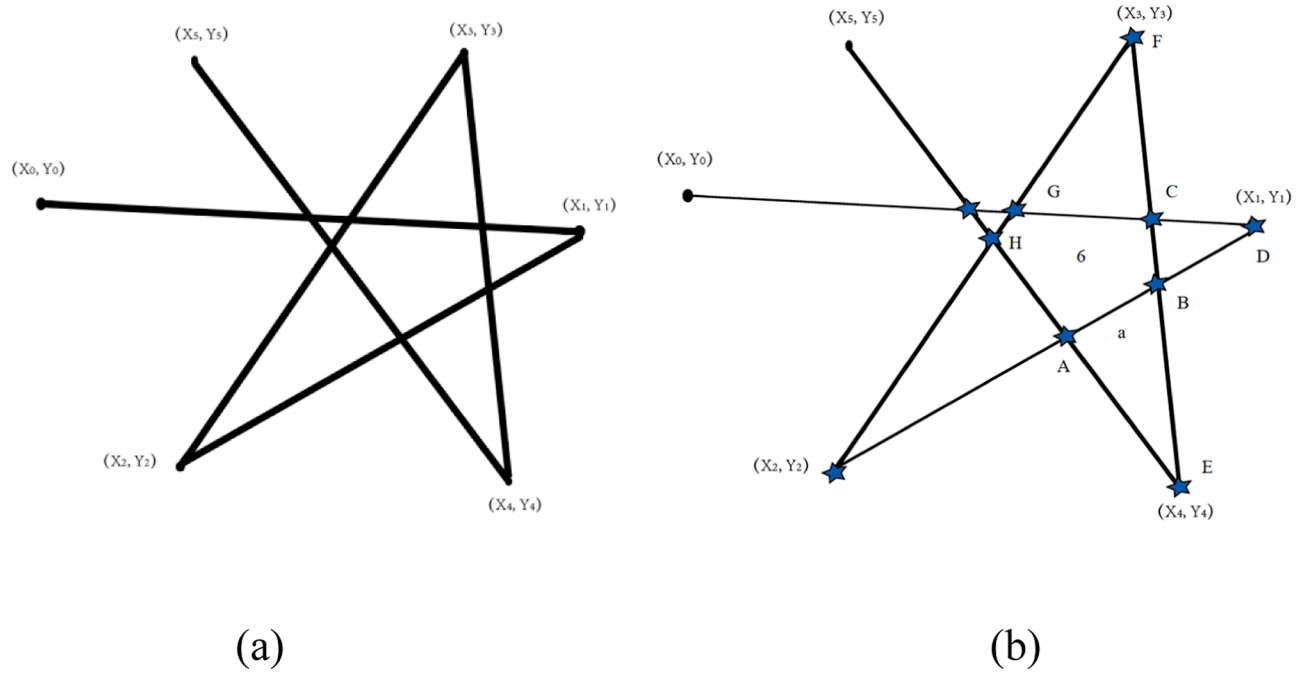

Figure 4. Pore size calculation process diagram: (a) web schematic diagram and (b) intersection points.

The computer should utilize a more complex algorithm to obtain the pore size of the simulated fibrous web. We drew a simple web schematic diagram to describe the algorithm. As shown in Figure 4a, five fiber segments are deposited on the collector. The bead coordinates (x_i, y_i) were predicted using our model. Six pores were enclosed by fiber segments. The pore size calculation should be performed after the computer recognizes six pores. Herein, we describe an algorithm for determining pore 6. Other pores can also be recognized using the same method.

First, the intersection points of these fiber segments (indicated by the asterisks in Figure 4b) were calculated. Two intersection points were randomly selected. For instance, "A" and "B" are shown in Figure 4b. Subsequently, the computer may randomly choose another point to constitute an edge with point "B". Thus, one of "BC", "BD", or "BE" may be generated. To recognize pore 6, "BC" is the correct selection. How do you avoid the selection of points "D" and "E"? We stipulate a constraint that the clockwise angle between "AB"

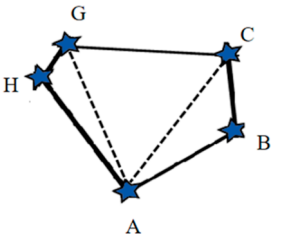

Figure 5. Segmentation of a pore.

https://doi.org/10.1021/acsomega.2c00276
ACS Omega 2022, 7, 20584−20595

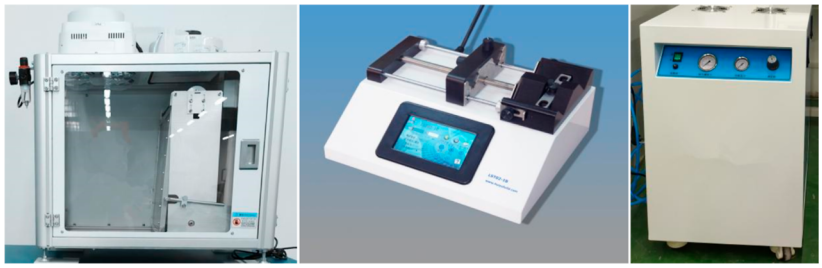

(a) (b) (c)

Figure 6. Characteristics of the SB machine: (a) spinning box; (b) propeller; and (c) air compressor.

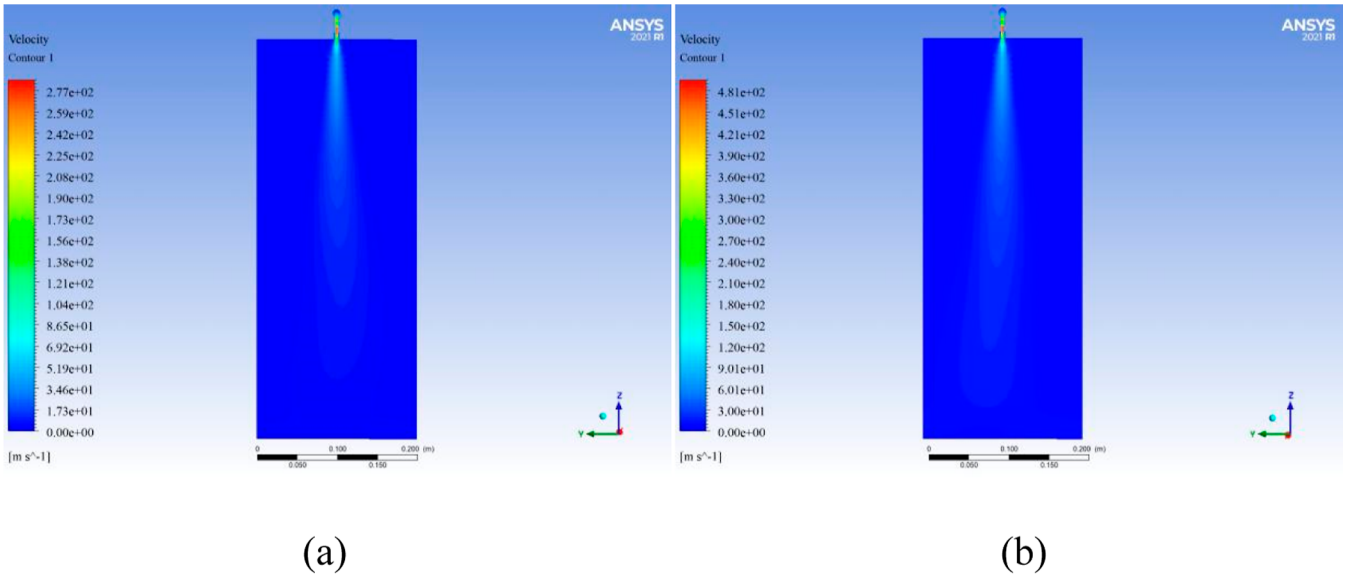

(a) (b)

Figure 7. (a) Velocity contour of simulated air flow (inlet pressure = 0.05 MPa) and (b) velocity contour of simulated air flow (inlet pressure = 0.15 MPa).

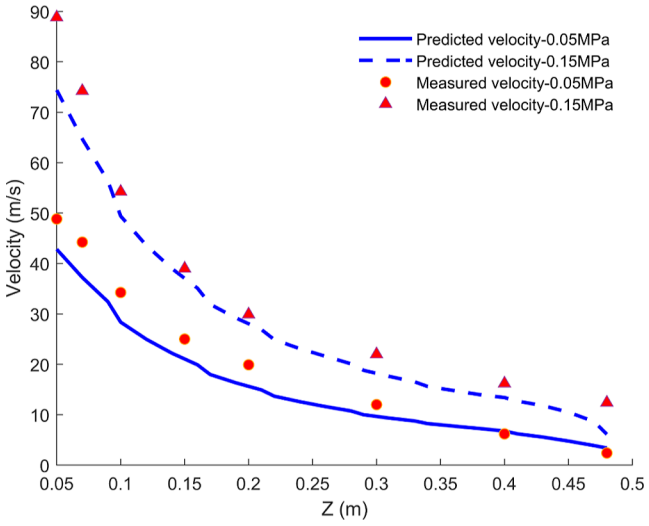

Figure 8. Simulated and experimental air velocities in the *z*-direction.

and the brand-new edge should be the smallest. Evidently, "D" fails to be chosen. However, the clockwise angle between "AB" and "BC" is the same as that of "AB" and "BE". To select "C", we additionally stipulate that the newly selected point should be anticlockwise relative to "AB". Therefore, the computer could successively select "G" from points "F" and "G" using the same method. The whole algorithm is repeated until the computer selects "A" again. Pore 6, which is enclosed by "ABCGH", was finally recognized.

After recognizing pore 6, the area of each pore was calculated to obtain the pore size. The pores can be separated into several triangles (Figure 5). For instance, the area of ΔACG can be calculated by

$$S_{ACG} = \frac{|\overrightarrow{AG} \times \overrightarrow{AC}|}{2} \tag{14}$$

Thus, the area of pore 6 is identical to the sum of ΔACG, ΔAGH, and ΔABC. The same method was used to calculate the area of all the pores. Thereafter, the pore diameter can be calculated by considering the pore as a circle. The calculated results are presented in Section 4.

Table 2. Processing Conditions for Fabrication

	sample A	sample B
pressure of air jet (Mpa)	0.15	0.05
nozzle to collector distance (NCD) (cm)	50	50
throughput rate of solution (mL/min)	0.3	0.3
diameter of the orifice (mm)	0.26	0.34
speed of the collector (cm/s)	2	4

https://doi.org/10.1021/acsomega.2c00276
ACS Omega 2022, 7, 20584−20595

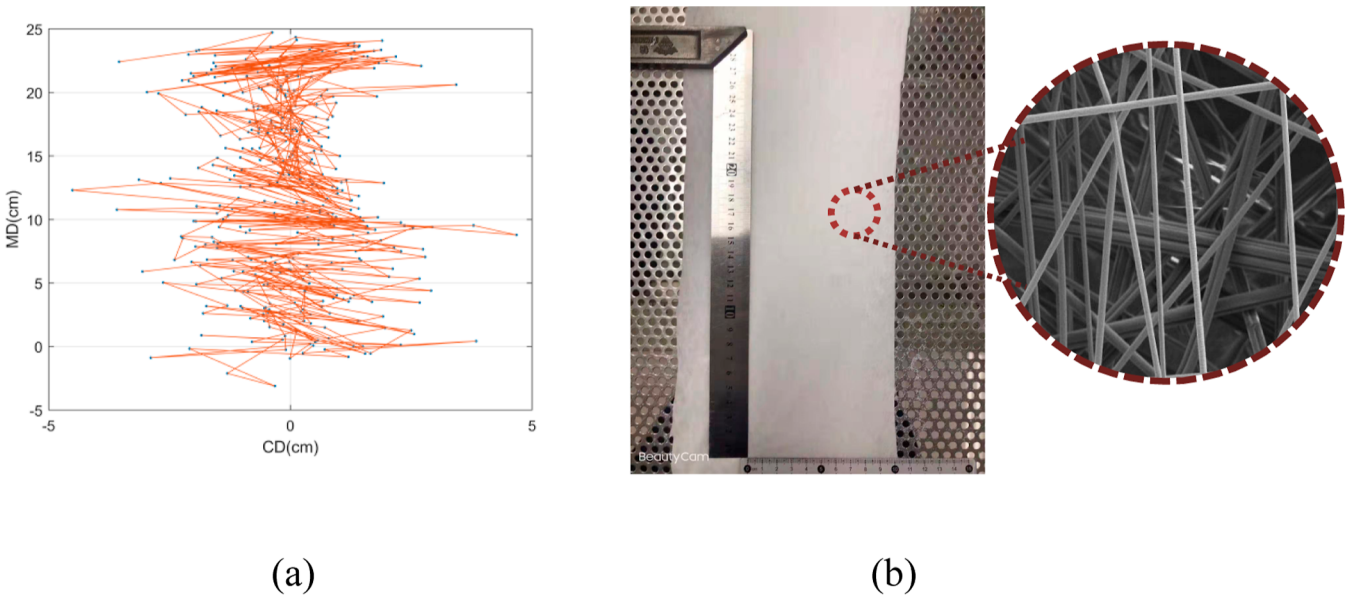

Figure 9. (a) Simulated fibrous web and (b) fabricated fibrous web.

3. EXPERIMENTAL SECTION

3.1. Verification of Simulated Air Flow. To verify the simulated results of air flow, we measured the air velocity in the z-direction under the nozzle using a hot-wire anemometer (model 55P11, Dantec Dynamics Inc., Denmark). The air flow speed changed drastically near the nozzle. Thus, the measurement positions were closely distributed near the nozzle but sparsely arranged away from the nozzle. To ensure the air flow is consistent with the simulation, the pressure of the ejected air jet was also set to 0.5 and 1.5 MPa.

3.2. Fibrous Web Fabrication and Structural Parameter Measurements. In Figure 6, the SB machine consists of a spinning box, pump, and air compressor. To verify the model, we fabricated two pieces of a fibrous web using an SB machine. The used polymeric solution was polyacrylonitrile (PAN)/dimethylacetamide (DMAC) with wt 12% PAN. All chemical reagents were purchased from the Sinopharm Group. The fabrication conditions are presented in Table 2.

After fabrication, the fibrous web was observed using a scanning electron microscope (SU8010, Hitachi, Ltd., Japan) and a microscope. The fiber diameter was determined based on scanning electron microscopy (SEM) images. The fiber orientation was measured using microscope photographs. The basis weight was measured following ISO 9073-1. The fibrous web was cut into 4 × 6 pieces. Thereafter, the pieces were weighed on a balance. The results were recorded to determine the basis weight distribution. The pore size of the fibrous web was measured using a capillary flow porometer (CFP-1100A, Porous Materials, Inc., USA). To avoid experimental errors, each measurement was performed thrice.

3.3. Measurement of the Evaporation Rate. Prior to SB, the PAN/DMAC solution mass m_s was weighed. Then, the generated fiber mat mass m_f was weighed again. According to assumption 4, the evaporation rate e_r could be simply estimated by

$$e_r = \frac{m_s - m_f}{m_s}/\mathrm{NCD} \tag{15}$$

4. RESULTS AND DISCUSSION

4.1. Simulated and Experimental Results of Air Flow. The SB air flow velocity distribution contours are shown in Figure 7. The predicted velocity curves and experimental results are shown in Figure 8. In Figure 7, it can be observed that the air jet is ejected from the SB nozzle and gradually

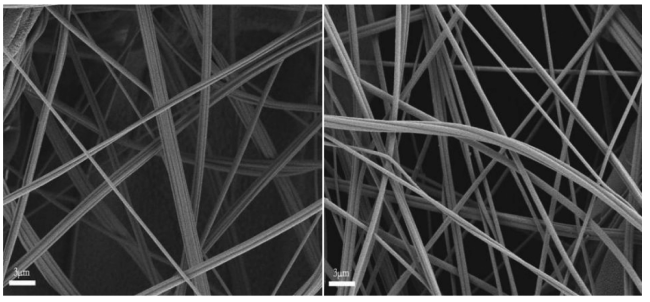

Figure 10. SEM photographs: (a) Sample A and (b) sample B.

Table 3. Distribution Characteristics of Predicted and Measured Parameters

	sample A		sample B	
	prediction	measurement	prediction	measurement
median diameter (μm)	0.32	0.4	0.34	0.45
diameter std.	0.0762	0.161	0.0859	0.178
median orientation (°)	93.92	94.02	90.49	90.51
orientation std.	31.77	40.00	30.94	46.02
total basis weight (mg)	43	47	29	31
MD basis weight std.	1.6	0.8	2.4	0.4
CD basis weight std.	8.4	9.2	9.6	7.6
median pore size (μm)	5.84	13.13	8.13	14.41

https://doi.org/10.1021/acsomega.2c00276
ACS Omega 2022, 7, 20584−20595

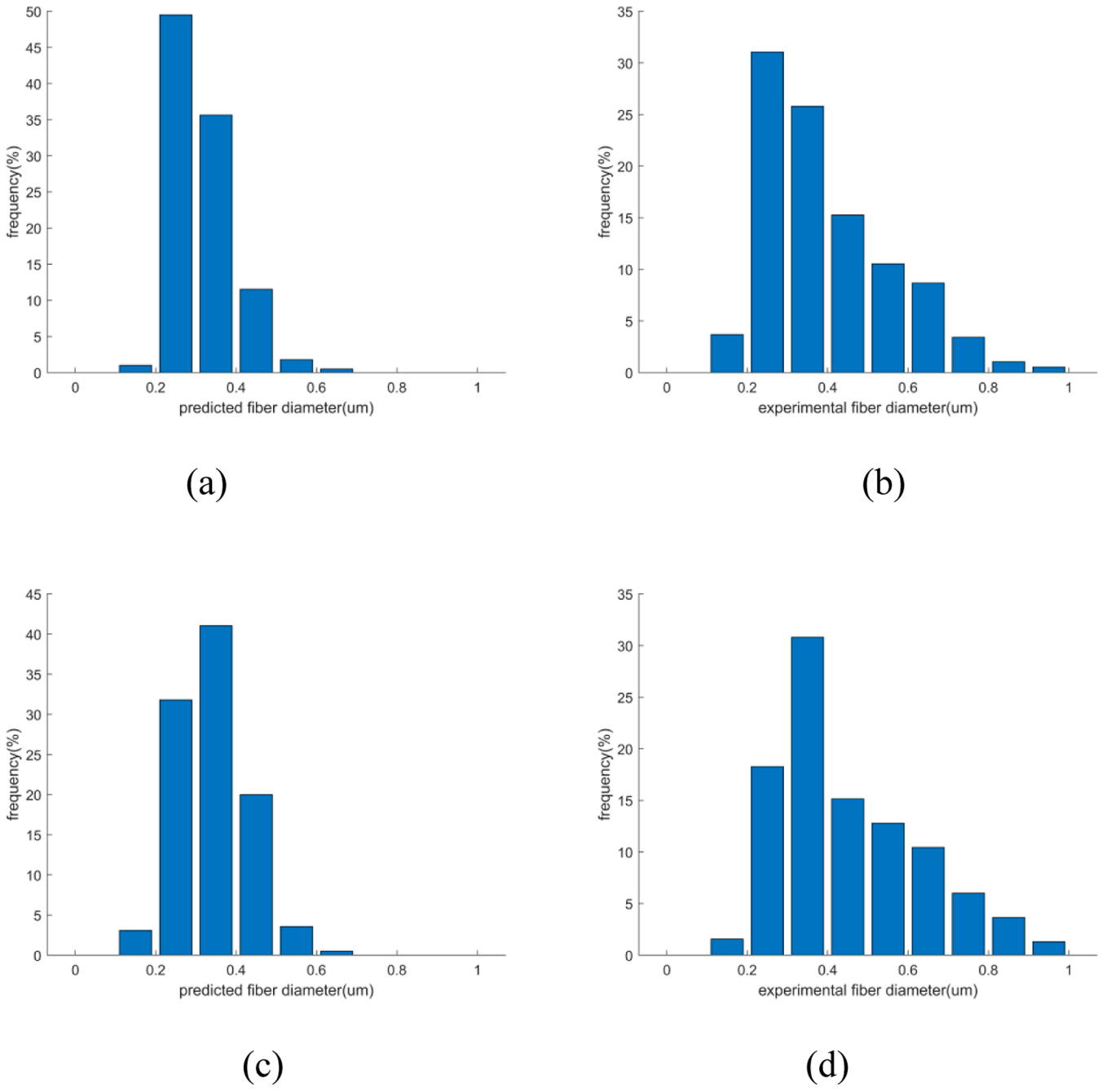

Figure 11. Predicted and measured fiber diameter distributions: (a) predicted diameter of sample A; (b) measured diameter of sample A; (c) predicted diameter of sample B; and (d) measured diameter of sample B.

spread in the opening environment; meanwhile, the speed of the air jet rapidly decayed. The experimental process was verified as follows: The air jet velocity was greater than the range of the hot-wire anemometer when $z < 0.05$ m. Additionally, because of the existence of the collector at $z = 0.5$ m and the difficulty in testing the air flow velocity on the flattened collector surface, the measureable domain of air-jet velocities was only $0.05 \text{ m} \leq z \leq 0.48$ m. Thus, the measured position along the thread line was at $z = 0.05$, 0.07, 0.1, 0.15, 0.2, 0.3, 0.4, and 0.48 m. Our experimental results were compared with the simulated results in Figure 8. It can be observed that the experimental and simulated data were in good agreement. The simulation results exhibited the characteristics of the air flow field. Therefore, we can still obtain the characteristics of the air flow field based on the simulated results, even without experimental data.

4.2. Mechanism of the Fibrous Web Structure Formation. The simulated and fabricated fibrous webs are shown in Figure 9 as an example. As shown in Figure 9a, the solution drops fell on the collector and generated a long strip distribution along the machine direction (MD). Figure 9b shows the fabricated web of the same size. Figure 10 shows the SEM images of the two fabricated samples. After cursory observation, it was found that the fiber diameter of sample B was larger than that of sample A. The fiber diameter distribution and formation reason are analyzed in Section 4.3.

4.3. Simulated and Experimental Structural Parameters of the Fibrous Web. In this section, we analyze the

https://doi.org/10.1021/acsomega.2c00276
ACS Omega 2022, 7, 20584−20595

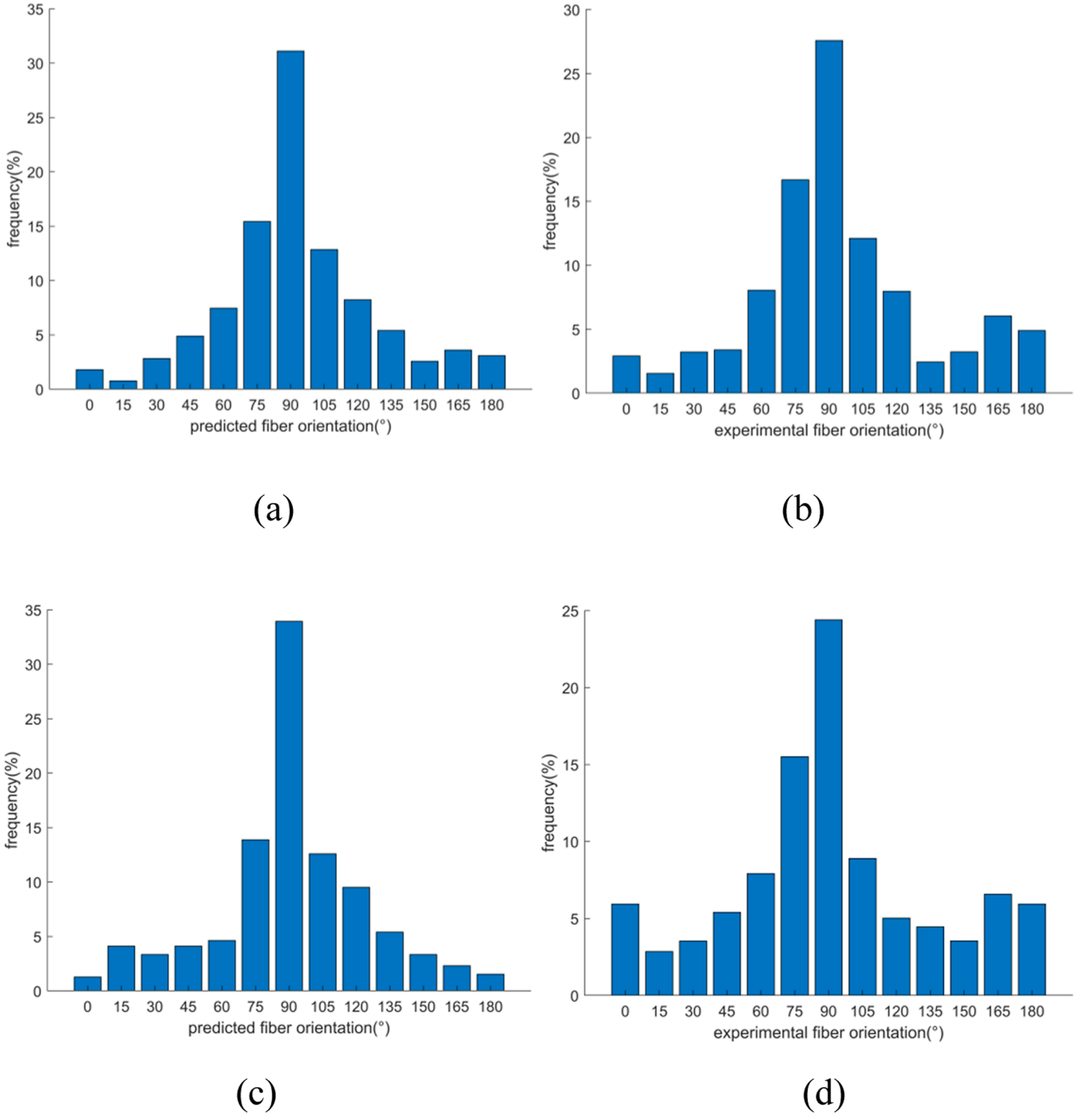

Figure 12. Predicted and measured fiber orientations: (a) predicted orientation of sample A; (b) measured orientation of sample A; (c) predicted orientation of sample B; and (d) measured orientation of sample B.

simulation results and the measured values of the fiber diameter, orientation, basis weight, and pore size. First, we have listed the distribution characteristics of the structural parameters in Table 3. These parameters are discussed in the following subsections.

4.3.1. Fiber Diameter. The predicted and measured fiber diameter distributions are shown in Figure 11. The median diameter and standard deviation (std.) are listed in Table 3. Both the predicted and measured results demonstrate that the fiber diameter is mainly distributed between 0.3 and 0.4 μm. The predicted results display a narrow distribution; however, the measured results are widely distributed. The relatively larger std. of the measured results listed in Table 3 also confirms the above description. Furthermore, thicker fibers (>0.5 μm) exist in the fabricated samples. This could be explained by fiber entanglement. The entangled parts increased the fiber diameter. However, given the complex contact and entanglement situation restricting the mechanistic study of fiber formation, our numerical model ignores fiber contact problems. In addition, compared with sample A, more thick fibers were collected in sample B because the air jet pressure employed in fabricating sample A is higher than that in fabricating sample B. This could also be attributed to the orifice size of sample A being smaller than that of sample B.

https://doi.org/10.1021/acsomega.2c00276
ACS Omega 2022, 7, 20584−20595

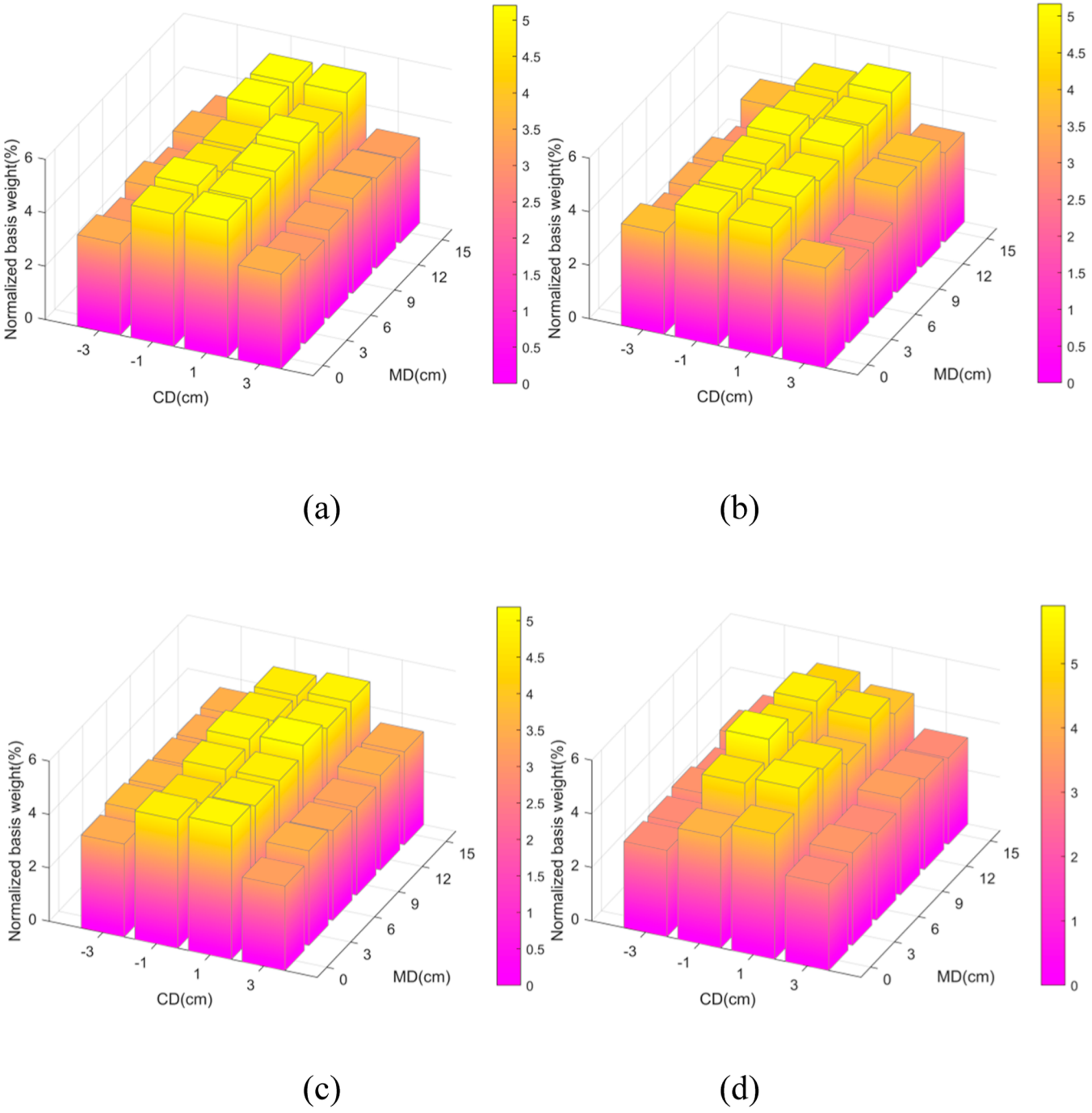

Figure 13. Predicted and measured basis weights: (a) predicted distribution of sample A; (b) measured distribution of sample A; (c) predicted distribution of sample B; and (d) measured distribution of sample B.

According to our observations, finer fibers were fabricated under higher air-jet pressures and smaller orifice sizes.

4.3.2. Fiber Orientation. The predicted and measured fiber orientation distributions are shown in Figure 12. The median orientation and std. are listed in Table 3. Both the predicted and measured results exhibited higher consistency. The fiber orientation was concentrated at approximately 90°. In this work, 90° was determined as the MD (the direction of the collector movement). Thus, both 0 and 180° represent CDs. The predicted and experimental results demonstrated that more fibers aligned along the MD. In SB, the fibers spread on the collector after they were blown onto the collector by the high-speed air jet. Owing to the collector movement, the fibers are subjected to friction and gradually arrange along the MD. The details of the friction are reported in our previous work.[13] In addition, two samples were fabricated on the collector at different speeds. Sample A was formed on a relatively slower collector than sample B. The median orientation of sample B is closer to 90° than that of sample A. When compared with the slower collector, the faster collector could fully arrange fibers along the MD, which generates more fibers with an orientation of approximately 90°.

4.3.3. Basis Weight. The predicted and measured basis weight distributions are shown in Figure 13. The total basis

https://doi.org/10.1021/acsomega.2c00276
ACS Omega 2022, 7, 20584−20595

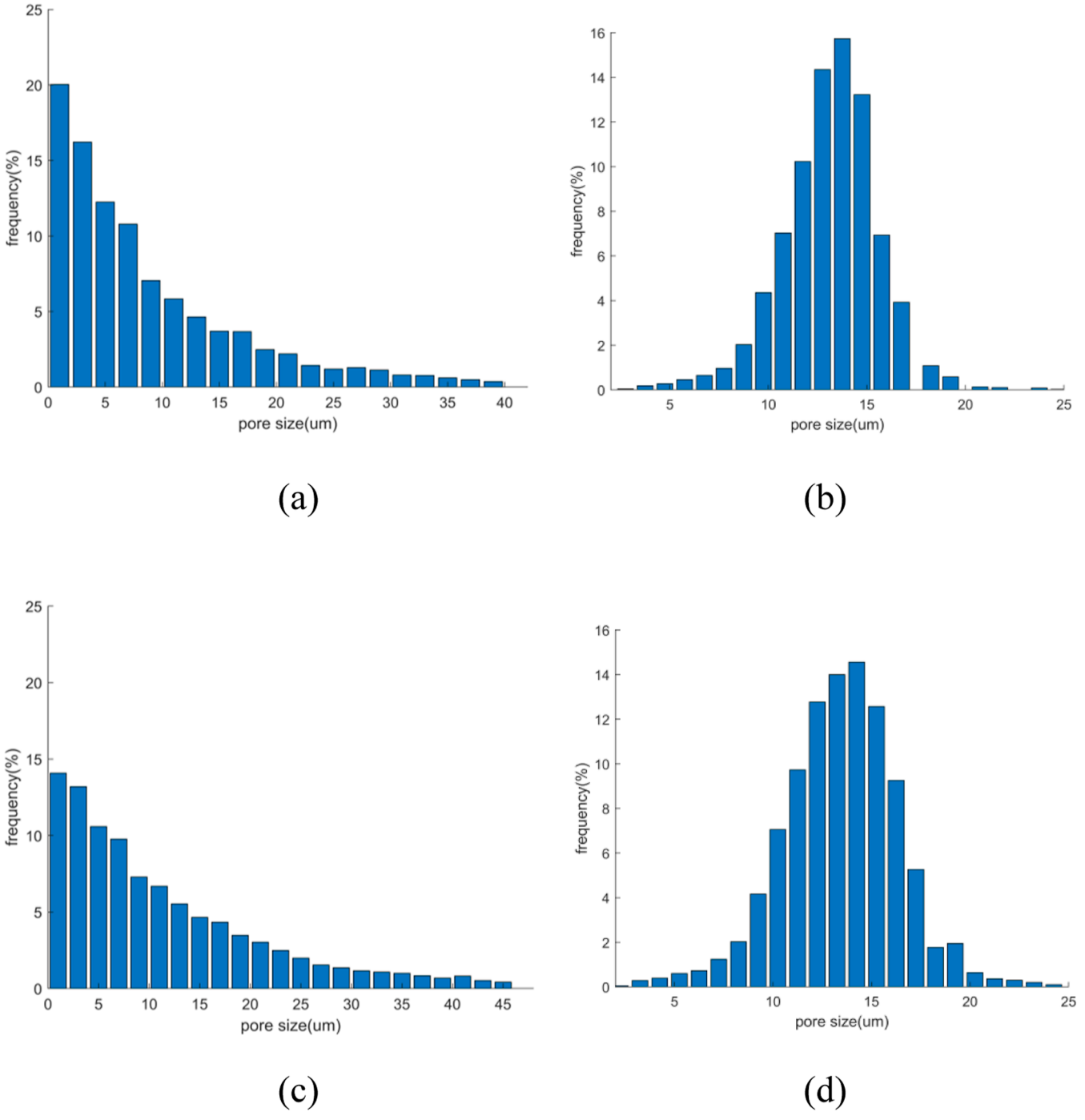

Figure 14. Predicted and measured pore size distributions: (a) predicted distribution of sample A; (b) measured distribution of sample A; (c) predicted distribution of sample B; and (d) measured distribution of sample B.

Figure 15. Side view of the pore morphology: (a) divided-pore and (b) through-pore and closed-pore.

https://doi.org/10.1021/acsomega.2c00276
ACS Omega 2022, 7, 20584−20595

weight and std. are listed in Table 3. The predicted and measured weights exhibited similar distributions. Solution drops tend to lay on the center of the fibrous web, which results in a heavier center part. Additionally, the std. in the MD was smaller than that in the CD. This implies that the weight of the fibrous web is distributed more evenly in the MD than in the CD, which is a common rule affirmed by Chhabra.[2] Continuous filaments fell on the moving collector and covered the thin part of the MD during SB. We have mentioned the uniformity difference of the basis weight in the MD and CD during MB in our previous work.[15−18] In this study, we also found a similar distribution of the basis weight during SB.

4.3.4. Pore Structure. As shown in Figure 14, the predicted and measured pore size distributions exhibited obvious differences. In Figure 14a,c, the pore size distribution exhibits a decreasing exponential distribution when the pore size increases. This confirms the existence of many relatively smaller pores (pore size < 5 μm) in the predicted samples. In Figure 14b,d, the measured pore size distribution displays a Gaussian-like distribution. The pore size was mainly concentrated around 15 μm. The median pore size in Table 3 also reflects this difference. The median pore size in the predicted sample was 5−8 μm, whereas in the experimental sample, it was 13−14 μm.

Our simulation algorithm was checked several times. Pore size measurements were also performed following the operating instructions. However, the predicted and measured sizes exhibited different distributions. Two reasons could explain this difference. First, given the predicted fibrous web in a two-dimensional (2D) space ignoring its thickness (Figure 9a), the fabricated fibrous web in a 3D space inevitably reveals the pore size difference. Figure 15a shows the details of this difference. The computer finds two pores because there exists another fiber across the original pore (it is displayed as a point in the side view). However, the porometer detects only one pore. The principle of the employed porometer is the bubble point method, which measures the pressure of liquid through the pore and then calculates the pore diameter based on the capillary effect equation. A fiber across the pore may affect the liquid pressure, but it cannot change the pore number during the measurement. Additionally, the liquid cannot flow through the closed pores (shown in Figure 10b); thus, the capillary flow porometer ignores massive closed pores.

Pore size evaluation is always a problem. The standard evaluation protocol is still absent among such methods, including mercury porosimetry, optical measurements, N_2 absorption, and small-angle X-ray scattering. Different results will be obtained for the same porous material by measuring with different types of instruments. However, the morphological diversity of the pores also directly affects the measured results. Our algorithm can count all pores without the influence of the pore morphology. We will further develop it into the 3D space to record a more realistic pore size in the future.

5. CONCLUSIONS

A numerical model was developed to reveal the SB web formation mechanism and predict the structural parameters, including the fiber diameter, fiber orientation, basis weight, and pore size. Compared with those made by MB, the fiber orientation and basis weight of fibers made by SB exhibit a similar distribution. However, there was a slight difference in the fiber diameter prediction because the fiber entanglement is ignored in this model. The fiber bundle generated by fiber entanglement affects the statistics of the fiber diameter. Conversely, the pore size distribution displays an extreme deviation between the predicted and measured sizes. This can be explained by the principle difference between the calculations and measurements. The deviation in the predicted results also indicates that our web morphology simulation in a 2D space still needs to be developed in three dimensions. We will continue to work on the web formation mechanism and provide improvements in the future..

AUTHOR INFORMATION

Corresponding Author

Yudong Wang − *College of Biological and Chemical Engineering, Guangxi University of Science and Technology, Liuzhou 545006, P. R. China;* orcid.org/0000-0002-7134-3495; Email: wangyudongwuqiao@163.com

Authors

Guangwu Sun − *Hainan Vocational University of Science and Technology, Haikou 571126 Hainan Province, P.R. China; College of Biological and Chemical Engineering, Guangxi University of Science and Technology, Liuzhou 545006, P. R. China; Jiangxi New Energy Technology Institute, Xinyu 338012 Jiangxi Province, P.R. China; School of Textiles and Fashion, Shanghai University of Engineering Science, Shanghai 201620, P. R. China;* orcid.org/0000-0001-8667-8119

Yinjiang Zhang − *College of Textile and Apparel, Key Laboratory of Clean Dyeing and Finishing Technology of Zhejiang Province, Shaoxing University, Shaoxing 312000 Zhejiang Province, P.R. China*

Wanli Han − *Materials and Textile Engineering College, Jiaxing University, Jiaxing 314001 Zhejiang Province, P. R. China;* orcid.org/0000-0002-1391-5504

Shanshan Shang − *School of Textiles and Fashion, Shanghai University of Engineering Science, Shanghai 201620, P. R. China;* orcid.org/0000-0002-4470-0207

Complete contact information is available at: https://pubs.acs.org/10.1021/acsomega.2c00276

Funding

Dr. Wang received funding from the Doctoral Fund Program of Guangxi University of Science and Technology (grant no. 21Z47). Dr. Han received funding from the Zhejiang Provincial Natural Science Foundation of China (grant no. LY22E060005). Dr. Shang received funding from the National Natural Science Foundation of China (grant no. 52106205).

Notes

The authors declare no competing financial interest.

NOMENCLATURE

m	mass of the solution segment
$\mathbf{F}_b$	restoring bending force
$\mathbf{F}_d$	air drag
$\mathbf{F}_{d,t}$	parallel drag force
$\mathbf{F}_{d,n}$	normal drag force
$\mathbf{F}_s$	friction
$\mathbf{F}_{ve}$	viscoelastic force
$\mathbf{F}_z$	the press generated by the air flow in the z direction
$\mathbf{G}$	gravity
$\mathbf{r}$	the spacial vector of the bead

https://doi.org/10.1021/acsomega.2c00276
ACS Omega 2022, 7, 20584−20595

d fiber diameter
l solution segment length
C_f air drag coefficient
C_{dn} air press coefficient
$\mathbf{v}_a$ air velocity
$\mathbf{v}_f$ solution velocity
g gravitational acceleration
k curvature of the solution segment
r lengthwise direction of the fiber
t simulation time
E elasticity modulus

GREEK LETTERS

ρ_a air density
ρ_f solution density
ψ bending force coefficient
$\boldsymbol{\sigma}$ tensile stress
γ friction coefficient.
μ solution dynamic viscosity

ABBREVIATIONS

SB solution blowing
MD machine direction
CD cross direction

REFERENCES

(1) Farias, R. M. d. C.; Menezes, R. R.; Oliveira, J. E.; de Medeiros, E. S. Production of Submicrometric Fibers of Mullite by Solution Blow Spinning (SBS). *Mater. Lett.* **2015**, *149*, 47.
(2) Li, L.; Kang, W.; Zhuang, X.; Shi, J.; Zhao, Y.; Cheng, B. A Comparative Study of Alumina Fibers Prepared by Electro-blown Spinning (EBS) and Solution Blowing Spinning (SBS). *Mater. Lett.* **2015**, *160*, 533.
(3) Zhuang, X.; Yang, X.; Shi, L.; Cheng, B.; Guan, K.; Kang, W. Solution Blowing of Submicron-scale Cellulose Fibers. *Carbohydr. Polym.* **2012**, *90*, 982.
(4) Rajgarhia, S. S.; Benavides, R. E.; Jana, S. C. Morphology Control of Bi-component Polymer Nanofibers Produced by Gas Jet Process. *Polymer* **2016**, *93*, 142.
(5) Bonan, R. F.; Bonan, P. R. F.; Batista, A. U. D.; Sampaio, F. C.; Albuquerque, A. J. R.; Moraes, M. C. B.; Mattoso, L. H. C.; Glenn, G. M.; Medeiros, E. S.; Oliveira, J. E. In vitro antimicrobial activity of solution blow spun poly(lactic acid)/polyvinylpyrrolidone nanofibers loaded with Copaiba (Copaifera sp.) oil. *Mater. Sci. Eng., C* **2015**, *48*, 372.
(6) Sabbatier, G.; Abadie, P.; Dieval, F.; Durand, B.; Laroche, G. Evaluation of an Air Spinning Process to Produce Tailored Biosynthetic Nanofibre Scaffolds. *Mater. Sci. Eng., C* **2014**, *35*, 347.
(7) Sinha-Ray, S.; Zhang, Y.; Yarin, A. L.; Davis, S. C.; Pourdeyhimi, B. Solution Blowing of Soy Protein Fibers. *Biomacromolecules* **2011**, *12*, 2357.
(8) Teno, J.; González-Gaitano, G.; González-Benito, J. Poly (ethylene-co-vinyl acetate) films prepared by solution blow spinning: Surface characterization and its relation with E. coli adhesion. *Polym. Test.* **2017**, *60*, 140.
(9) Hsiao, H.-Y.; Huang, C.-M.; Hsu, M.-Y.; Chen, H. Preparation of High-surface-area PAN-based Activated Carbon by Solution-blowing Process for CO2 Adsorption. *Sep. Purif. Technol.* **2011**, *82*, 19.
(10) Zhuang, X.; Shi, L.; Jia, K.; Cheng, B.; Kang, W. Solution Blown Nanofibrous Membrane for Microfiltration. *J. Membr. Sci.* **2013**, *429*, 66.
(11) Bilbao-Sainz, C.; Chiou, B.-S.; Valenzuela-Medina, D.; Du, W.-X.; Gregorski, K. S.; Williams, T. G.; Wood, D. F.; Glenn, G. M.; Orts, W. J. Solution Blow Spun Poly(lactic acid)/hydroxypropyl Methylcellulose Nanofibers with Antimicrobial Properties. *Eur. Polym. J.* **2014**, *54*, 1.
(12) Sinha-Ray, S.; Sinha-Ray, S.; Yarin, A. L.; Pourdeyhimi, B. Theoretical and Experimental Investigation of Physical Mechanisms Responsible for Polymer Nanofiber Formation in solution blowing. *Polymer* **2015**, *56*, 452.
(13) Sun, G. W.; Song, J.; Xu, L.; Wang, X. H. Numerical Modelling of Microfibers Formation and Motion during Melt Blowing. *J. Text. Inst.* **2018**, *109*, 300.
(14) Sun, G.; Yang, J.; Sun, X.; Wang, X. Simulation and Modeling of Microfibrous Web Formation in Melt Blowing. *Ind. Eng. Chem. Res.* **2016**, *55*, 5431.
(15) Sun, G.; Ruan, Y.; Wang, X.; Xin, S.; Chen, Y.; Hu, W. Numerical Study of Melt-blown Fibrous Web Uniformity Based on the Fiber Dynamics on a Collector. *Ind. Eng. Chem. Res.* **2019**, *58*, 23519.
(16) Sun, G.; Liu, R.; Shang, S.; Xin, S.; Wang, X.; Gao, W.; Hu, W. Association study between basis weight distribution of melt-blown web and air velocity distribution on the collector. *J. Ind. Text.* **2019**, *51*. DOI: 10.1177/1528083719888676.
(17) Sun, G.; Yang, J.; Xin, S.; Yu, R.; Wang, X. Influence of Processing Conditions on the Basis Weight Uniformity of Melt-blown Fibrous webs: Numerical and Experimental study. *Ind. Eng. Chem. Res.* **2018**, *57*, 9707.
(18) Wang, Y.; Qiu, Y.; Ji, C.; Wang, X.; Guan, F. The Effect of the Geometric Structure of the Modified Slot Die on the Air Field Distribution in the Meltblowing Process. *Text. Res. J.* **2022**, *92*, 423.
(19) Ji, C.; Wang, Y.; Sun, Y. Numerical Investigation on a Melt-blowing Die with Internal Stabilizers. *J. Ind. Text.* **2021**, *50*, 1409.
(20) Tan, D. H.; Herman, P. K.; Janakiraman, A.; Bates, F. S.; Kumar, S.; Macosko, C. W. Influence of Laval Nozzles on the Air Flow Field in Melt Blowing Apparatus. *Chem. Eng. Sci.* **2012**, *80*, 342−348.
(21) Sun, G.; Chen, Y.; Ruan, Y.; Li, G.; Hu, W.; Xin, S. Modeling and Experimental Study of Pore Structure in Melt-blown Fiber Assembly. *J. Ind. Text.* **2021**, 15280837211011776.
(22) Krutka, H. M.; Shambaugh, R. L.; Papavassiliou, D. V. Analysis of the Temperature Field from Multiple Jets in the Schwarz Melt Blowing Die Using Computational Fluid Dynamics. *Ind. Eng. Chem. Res.* **2006**, *45*, 5098.
(23) Akhlaghi, O.; Menceloglu, Y. Z.; Akbulut, O. Rheological Behavior Of Poly(Acrylonitrile) Concentrated Solutions: Effect Of Sb2O3 Nanoparticles on Shear And Extensional Flow. *Colloid Polym. Sci.* **2016**, *294*, 1463−1473.
(24) Dong, Y.; Kong, J.; Mu, C.; Zhao, C.; Thomas, N. L.; Lu, X. Materials Design Towards Sport Textiles with Low-friction and Moisture-wicking Dual Functions. *Mater. Des.* **2015**, *88*, 82.

https://doi.org/10.1021/acsomega.2c00276
ACS Omega 2022, 7, 20584−20595